ARMY RESEARCH LABORATORY

Adaptive Target Detection in FLIR Imagery Using the Eigenspace Separation Transform and Principal Component Analysis

by S. Susan Young, Heesung Kwon, and Nasser M. Nasrabadi

ARL-TR-3544 June 2005

NOTICES

Disclaimers

The findings in this report are not to be construed as an official Department of the Army position unless so designated by other authorized documents.

Citation of manufacturer's or trade names does not constitute an official endorsement or approval of the use thereof.

Destroy this report when it is no longer needed. Do not return it to the originator.

Army Research Laboratory
Adelphi, MD 20783-1197

ARL-TR-3544 **June 2005**

Adaptive Target Detection in FLIR Imagery Using the Eigenspace Separation Transform and Principal Component Analysis

S. Susan Young, Heesung Kwon, and Nasser M. Nasrabadi
Sensors and Electron Devices Directorate, ARL

REPORT DOCUMENTATION PAGE

Form Approved
OMB No. 0704-0188

1. REPORT DATE *(DD-MM-YYYY)*	2. REPORT TYPE	3. DATES COVERED (From - To)
June 2005	Final	

4. TITLE AND SUBTITLE
Adaptive Target Detection in FLIR Imagery Using the Eigenspace Separation Transform and Principal Component Analysis

5a. CONTRACT NUMBER

5b. GRANT NUMBER

5c. PROGRAM ELEMENT NUMBER

6. AUTHOR(S)
S. Susan Young, Heesung Kwon, and Nasser M. Nasrabadi

5d. PROJECT NUMBER

5e. TASK NUMBER

5f. WORK UNIT NUMBER

7. PERFORMING ORGANIZATION NAME(S) AND ADDRESS(ES)
U.S. Army Research Laboratory
ATTN: AMSRD-ARL-SE-SE
2800 Powder Mill Road
Adelphi, MD 20783-1197

8. PERFORMING ORGANIZATION REPORT NUMBER
ARL-TR-3544

9. SPONSORING/MONITORING AGENCY NAME(S) AND ADDRESS(ES)
U.S. Army Research Laboratory
2800 Powder Mill Road
Adelphi, MD 20783-1197

10. SPONSOR/MONITOR'S ACRONYM(S)

11. SPONSOR/MONITOR'S REPORT NUMBER(S)

12. DISTRIBUTION/AVAILABILITY STATEMENT
Approved for public release; distribution unlimited.

13. SUPPLEMENTARY NOTES

14. ABSTRACT
In this paper, an adaptive target detection algorithm for forward-looking infrared (FLIR) imagery is proposed which is based on measuring differences between structural information within a target and its surrounding background. At each pixel in the image a dual window is opened where the inner window (inner image vector) represents a possible target signature and the outer window (consisting of a number of outer image vectors) represents the surrounding scene. These image vectors are then preprocessed by two directional highpass filters to obtain the corresponding image gradient vectors. The target detection problem is formulated as a statistical hypotheses testing problem by mapping these image gradient vectors into two linear transformations, P_1 and P_2 and, via principal component analysis and eigenspace separation transform, respectively. The first transformation P_1 is only a function of the inner image gradient vector. The second transformation P_2 is a function of both the inner and outer image gradient vectors. For the hypothesis H_1 (target): the difference of the two functions is small. For the hypothesis H_0 (clutter): the difference of the two functions is large. Results of testing the proposed target detection algorithm on two large FLIR image databases are presented.

15. SUBJECT TERMS
target detection, eigenvector analysis, eigenspace separation transform, principal component analysis, FLIR imagery, statistical hypotheses testing

16. SECURITY CLASSIFICATION OF:			17. LIMITATION OF ABSTRACT	18. NUMBER OF PAGES	19a. NAME OF RESPONSIBLE PERSON
a. REPORT	b. ABSTRACT	c. THIS PAGE			S. Susan Young
Unlcassified	Unclassified	Unclassified	SAR	26	19b. TELEPHONE NUMBER (*Include area code*) 301-394-0230

Contents

List of Figures

List of Tables

1. Introduction

The structural information of man-made targets (ground-based vehicles) in forward-looking infrared (FLIR) imagery appears different from that of their surrounding background. Automatic target detection techniques use the radiated energy from a man-made target in FLIR imagery to detect targets (*1-2*). Energy distribution patterns on the targets are determined by the operational conditions of the vehicles, weather conditions and solar loading, atmospheric conditions, and other factors. Similarly, the apparent temperature of background objects is determined by environmental conditions.

The research work in infrared imaging system and automatic target detection/recognition (ATD/R) were started approximately at the same time nearly 40 years ago; see the review paper by Ratches et al., (*3*). The survey papers by Bhanu (*4-5*) summarize various algorithms for ATD/R in static FLIR images that were developed up to early 1990s; these algorithms predominately use traditional image processing approaches for (optical) picture processing. Since early 1990s, combinations (or mixtures) of classical/traditional image processing and emerging techniques have been proposed for the FLIR target detection problem. For instance, the traditional approach of segmenting the target from the background still draws attention of the FLIR researchers. Meanwhile, various emerging techniques are also being studied in segmentation algorithm. For example, Sang et al., (*6*) use Hopfield neural network with edge constraint, and Sun et al., (*7*) exploit fuzzy thresholding and edge detection in their segmentation algorithms.

There have also been studies of "matched filtering" algorithms that assume a specific shape/model for the FLIR signature of a man-made target. For instance, Erinsse et al., (*8*) use DOG (difference of Gaussian) filter as a bandpass filter to enhance the signature of man-made targets in FLIR imagery, and use the resultant information to detect ("pull") these targets. Park et al., (*9*) assume that a man-made target exhibits a peak response when a Mexican hat filter is applied to FLIR imagery; in this case, the Mexican hat filter is used as the mother wavelet of the multidimensional wavelets. The filtered image is thresholded to obtain the location of man-made targets. Zhou et al., (*10*) use five simple matching patterns (shapes of rectangle, square, oval, rounded-rectangle, and circle) for all targets. They applied the Gabor function (a sinosoidal function weighted by a Gaussian function) to both their matching patterns and the IR image to generate Gabor feature vectors. The similarity measure between the Gabor feature vector at each image point and that of the matching patterns is calculated. The similarity values are then thresholded to obtain the locations of the targets. Weber et al., (*11*) use six Gabor function filters; these are two directional RGFs (real Gabor functions) to detect object height and width and four directional IGFs (imaginary Gabor functions) to detect the left, right, top and bottom edges of the object. The input image is correlated with each of the six Gabor filters, and these

six correlation outputs are then quadratically combined; the final detection is performed using a threshold.

Neural network technologies are usually used as a classifier for an automatic target recognition system; see Roth (*12*) and Rizvi et al., (*13*) for a survey. Neural networks have also been exploited to classify each pixel in the FLIR imagery as either man-made structures or background (clutter) in order to detect targets. For example, see the articles by Dwan et al., (*14*) and Ramanan et al., (*15*).

Multiscale fractal method is another emerging technique that has been used for FLIR target detection. Xue et al., (*16*) compute fractal dimensions through several resolution levels of an image. The K-mean method is then used to classify the target and background based on the resultant fractal dimensions. Shekarforoush et al., (*17*) have also used a multi-fractal formalism for object detection and tracking in FLIR sequences.

The apparent temperature contrast between a man-made target and its surrounding is a key factor in most FLIR target detection algorithms. A target with high contrast (temperature) is relatively easy to detect; this property is exploited by most of the above-mentioned algorithms. However, for low contrast targets, some form of structural information needs to be exploited. In most of the above-mentioned algorithms, the image characteristics are globally analyzed either in the filtering operation or in the feature extraction process. This is achieved by comparing the pixels representing the target with the other pixels in the entire image. This global-based approach neglects the local variations between the signatures of the target and its surrounding medium. Some researchers have used double-gated filters that exploit these local variations for target detection: see Gregoris et al., (*18*) and Der et al., (*19*). In these methods, the authors identify an inner target window surrounded by an outer window. The inner window carries information on the FLIR signature properties of the target zone, and the outer window is used to identify the signature properties of the nearby background. In reference (*18*), a filter is used to measure the difference in the mean pixel values of the inner target window and the outer background window, and the pixel standard deviation in the background window. The ratio of the mean difference to the standard deviation, that is, a "normalized" mean difference, is compared to a pre-assigned threshold. The inner windows with ratios exceeding the threshold are labeled as possible man-made targets. In reference (*19*), more comprehensive features (such as contrast difference, gradient strength, straight edge information, etc.) are computed from the inner window and the outer window, and exploited for target detection purposes.

In this paper, the local similarity measure between the inner and outer window is used to explore the differences between structural information of a target and its surrounding scene in FLIR imagery. Due to the signature variability of FLIR images, the presence of individual structural patterns, such as edges, shapes, textures, etc., cannot be reliably predicted. We use an eigenspace analysis to represent the variations of the structural information of a target and its background. We first construct the inner and outer image vectors that represent the multi-

dimensional signal properties of the FLIR signatures of the target and its background, respectively. While the inner image vector is solely constructed from the inner window (box), the outer image vectors are constructed from a more extended outer window that consists of many overlapping outside boxes that are of the same size as the inner box. These two image vectors are then processed by two directional gradient operators. The resulting image gradient vectors are mapped by two transformations, P_1 and P_2, via principle component analysis (PCA) and the eigenspace separation transform (EST) (*20*), respectively. The first transformation P_1 is a function of the inner image vector. The second transformation P_2 is a function of both the inner and outer image vectors. The target detection problem is formulated as a statistical hypothesis testing problem. That is, for the hypothesis H_1 (inner image vector is a target): the difference between the components of P_1 and P_2 is small. For hypothesis H_0 (inner image vector is clutter): the difference between these two functions is large.

This paper is organized as follows. The image feature set is described in section 2 using image vector construction and gradient signals. The adaptive target detection algorithm is discussed in section 3, where EST and PCA are outlined, and the hypotheses and target detection procedure are presented in detail. In section 4, results of testing the proposed algorithm on two large FLIR image databases are presented using ROC (receiver operation characteristics) curves. The proposed algorithm is also compared with other detection algorithms. Conclusions are given in section 5.

2. FLIR Imagery Feature Set

In this section, we describe how the image vectors are constructed to represent both a target region and it surrounding scene. Directional gradient filters are used to preprocess the image vectors. The resulting gradient image vectors are used as the feature set in our target detection algorithm.

2.1 Image Vectors

For a given pixel in the image, a window (called inner box) centered at the pixel is constructed as shown in figure 1. The size of the inner box is determined by the largest target size in the target library, which is based on a known or estimated range. Similarly, an outer window, X_{out}, as shown in figure 1, is constructed by a bigger window that surrounds but does not include the inner window. The size of the outer window in our implementation is three times the width and height of the inner window. The outer window is then partitioned into N small overlapping outer boxes (shift by 1 pixel in x or y direction) which have the same size as the inner box. The inner image vector that is denoted by X_{in} is the vectorized image data of the inner box. It is written as

$$X_{in} = [x_1, x_2, \cdots, x_m]$$

Where $m = w \times h$, w and h are the width and height of the inner box, and x_j is the image pixel value, $j = 1,2,\ldots,m$.

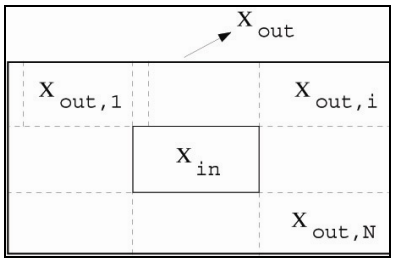

Figure 1. Image vectors construction.

The outer window, X_{out}, which contains N smaller outer boxes represented by $x_{out,i}$ where $i = 1,2,\ldots,N$. Each of the N small outer boxes is the vectorized image data representing each of N overlapping boxes that have the same dimension m as the inner box. It is written as

$$X_{out} = [x_{out,1}, x_{out,2}, \cdots, x_{out,N}]$$

$$x_{out,i} = [y_1 y_2, \cdots y_m], \quad i = 1,2,\cdots, N$$

where y_j is the image pixel value, $j = 1,2,\ldots,m$.

2.2 Gradient Image

The performance of many image processing algorithms is improved by first applying gradient operators to enhance the edge information within the image. Many studies of the human visual system provide evidence that the brain extracts edge and motion information early in the visual processing (*21-22*). Our experiments likewise show that the proposed algorithm performs much better using the gradient images than the pixel gray levels of the original FLIR imagery.

Two gradient images are formed by passing the input image through two directional high pass filters. Filter F_h is designed to high pass filter the image in the horizontal direction x. Similarly, F_v is the vertical high pass filter used to enhance the vertical edges in the y direction. The two directional high pass filters are defined as two separable differentiation operations, that is,

$$F_h = 1/2[-1 \quad 1]; \quad F_v = 1/2\begin{bmatrix} -1 \\ 1 \end{bmatrix}.$$

Examples of gradient images are shown in figure 2. Note that the gradient (edge) information about the target (truck) in all directions is preserved. However, the edge information about hot roads are suppressed in the x direction but emphasized in the y direction. Usually a target contains edge information in all directions. The background scene might only contain edge information in a particular direction. In this paper, the gradient images in both directions are passed to the detection technique where a detection decision is made by using the detection result from both of the input gradient images.

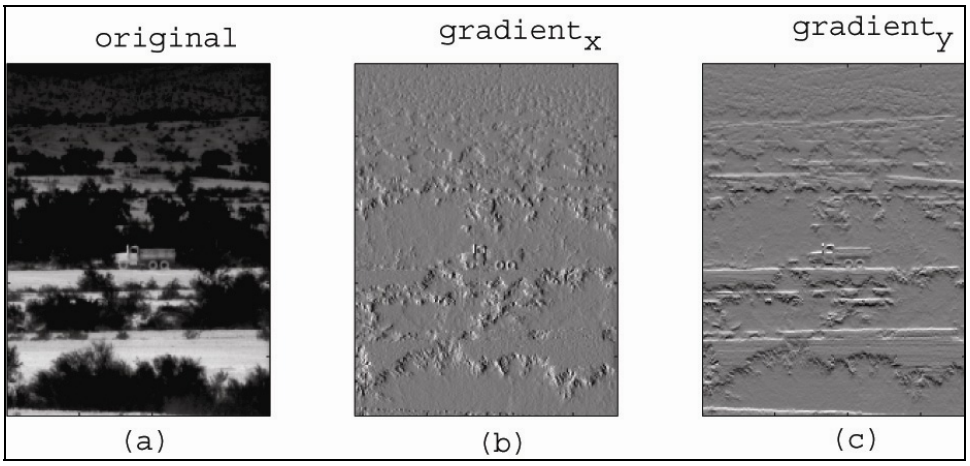

Figure 2. Examples of gradient images: (a) original image, (b) gradient image obtained by the highpass filtering in the *x* direction, and (c) gradient image obtained by the highpass filtering in the *y* direction.

3. Adaptive Detection of Target in FLIR Imagery

The two image vectors X_{in} and X_{out} that were defined above are mapped into two transformations $P_1(X_{in})$ and $P_2(X_{in}, X_{out})$ via EST and PCA, respectively. Note that $P_1(X_{in})$ is a function of X_{in} only, while $P_2(X_{in}, X_{out})$ is a function of X_{in} and X_{out}.

The target detection problem is formulated as a hypothesis test. For hypothesis H_1: target being within the inner box, the difference between $P_1(X_{in})$ and $P_2(X_{in}, X_{out})$ should be small. For hypothesis H_0: clutter being within the inner box, the difference between these two functions should be large. That is:

$$H_0 = \left|P_1(X_{in}) - P_2(X_{in}, X_{out})\right|^2 > \delta \tag{1}$$

$$H_1 = \left|P_1(X_{in}) - P_2(X_{in}, X_{out})\right|^2 < \delta$$

where δ is pre-selected as a threshold. The two functions $P_1(X_{in})$ and $P_2(X_{in}, X_{out})$ that are obtained via EST and PCA are discussed in the following subsection.

3.1 EST and PCA

The EST has been proposed by Torrieri as a preprocessor to a neural binary classifier in (*20*). The EST calculates the difference covariance matrix C

$$C = C_{out} - C_{in}$$

where C_{out} and C_{in} are the covariance matrices of the outer and inner image vectors, respectively. That is,

$$C_{in} = \left[X_{in} - \mu_{X_{in}}\right]\left[X_{in} - \mu_{X_{in}}\right]^T$$

$$C_{out} = \frac{1}{N}\sum_{i=1}^{N}\left[X_{out,i} - \mu_{X_{out,i}}\right]\left[X_{out,i} - \mu_{X_{out,i}}\right]^T$$

where μ_x is the mean value of either $x = X_{in}$ or $x = X_{out,i}$. N is the number of small outer boxes forming the outer window. The eigenvalues and eigenvectors of difference covariance matrix C are calculated. Some of these eigenvectors are associated with the positive eigenvalues. They are referred to as EST positive eigenvectors V_{est+}. The eigenvectors associated with the negative eigenvalues are referred to as EST negative eigenvectors V_{est-}. Based on the eigenvector properties, all EST positive and negative eigenvectors are orthogonal to each other. The positive eigenvectors V_{est+} mainly represent the outer image vector subspaces. Similarly, the negative eigenvectors V_{est-} represent the inner image vector subspaces. In the design of the covariance matrix in this paper, only one inner image vector forms the inside covariance matrix, so there is only one non-zero EST negative eigenvector.

An example of showing EST property is illustrated in figure 3, where two target chips (truck and tank) are considered as the outer and inner image vectors, respectively. In this example, the truck image is considered as the outer image vector (however, in a real scenario, it would be a clutter chip), while the tank image is considered as the inner image vector. The original images of the truck and tank are shown in figures 3a-b. The positive eigenvector V_{est+} and the negative eigenvector V_{est-} are shown in figures 3c-d. From figure 3, we can observe that V_{est+} contains truck and the shadow of the tank. The negative eigenvector V_{est-} contains mainly tank but the shadow of the truck is still visible.

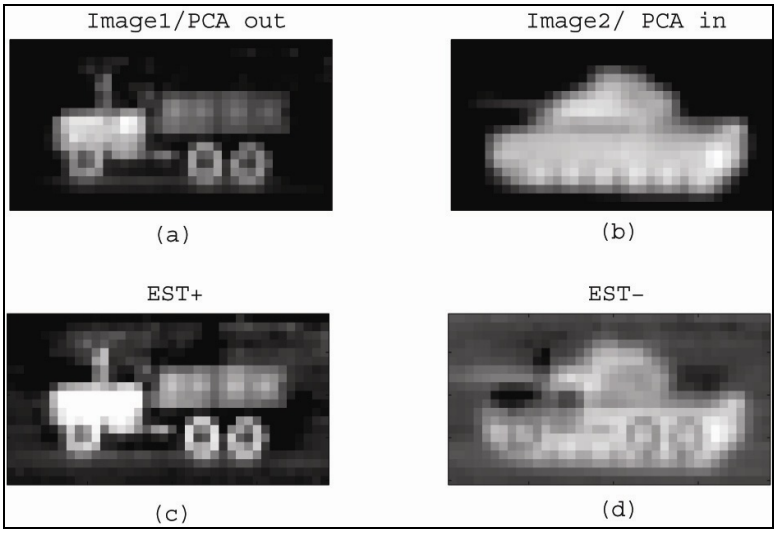

Figure 3. Examples of EST and PCA.

In PCA analysis, the eigenvectors of the inside covariance matrix C_{in} and outside covariance matrix C_{out} are calculated separately. We call the eigenvectors obtained from C_{out} PCA outside eigenvectors $V_{pca,out}$. Similarly, the eigenvectors obtained from C_{in} are called PCA inside eigenvectors $V_{pca,in}$. PCA inside eigenvector $V_{pca,in}$ is, of course, not expected to be orthogonal to PCA outside eigenvectors $V_{pca,out}$. Since there is only one inner image vector to form the inside covariance matrix, there is only one non-zero PCA inside eigenvector. Therefore, $V_{pca,in}$ is the normalized version of X_{in}, that is,

$$V_{pca,in} = \beta X_{in}$$

where β is the square root of the energy (norm) of the inner image vector, which is the same as the corresponding eigen value.

3.2 Hypotheses

A visual motivation for the formulation in equation 1 is illustrated in figure 4. For simplicity, assume that the outer window consists of only two vectors, $X_{out,1}$ and $X_{out,2}$. The inner image vector is X_{in}, which is aligned in the same direction as the PCA inside eigenvector $V_{pca,in}$. After the EST procedure, the positive and negative eigenvectors V_{est+1}, V_{est+2}, and V_{est-} are aligned approximately with the inner and outer image vectors, respectively. In addition, all positive and negative eigenvectors are orthogonal to each other.

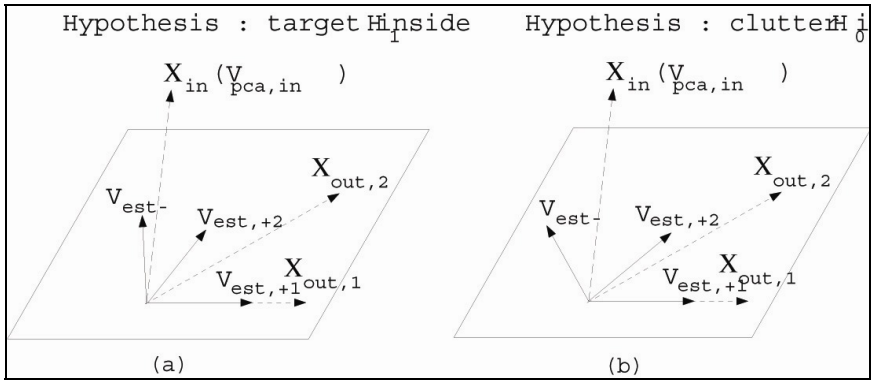

Figure 4. Visualization of hypotheses.

Consider the EST properties as demonstrated by the results in figure 3. The negative EST eigenvector predominately exhibits features that originally appear in the inner window (the tank) and the positive EST eigenvector contains the features that appear mainly in the outer window (the truck). Thus, the negative and positive EST eigenvectors approximately align with the inner and outer windows, respectively. We use these properties for our hypothesis testing problem in the following fashion. For hypothesis H_0, where clutter is within the inner box, the re-alignment of EST eigenvectors with respect to the PCA eigenvectors causes the negative EST eigenvector V_{est-} to be distant from the PCA inside eigenvector $V_{pca,in}$. For hypothesis H_1, where the target is

within the inner box, the EST negative eigenvector V_{est-} is more closely aligned to the PCA inside eigenvectors $V_{pca,in}$.

When there is clutter within the inner box that is somewhat similar to its surroundings, the difference between the inner and outer image vectors is not large. The EST procedure mixes the inner and outer image vectors and generates the positive and negative eigenvectors. The EST positive eigenvectors present mainly the subspace corresponding to the outer image vectors, which are also similar to the inner clutter image vector. Because the EST negative eigenvector has to be orthogonal with the EST positive eigenvectors, the EST negative eigenvector is more distant from the inner image vector. This causes the residual energy between the EST negative eigenvector V_{est-} and the PCA inside eigenvector $V_{pca,in}$ to be large. On the other hand, when there is a target in the inner box, there is a larger difference between the inner and outer image vectors. The EST negative eigenvector is generated to be orthogonal with the EST positive eigenvectors, which are already very different from the inner image vector. The EST negative eigenvector is then closer to the inner image vector that is proportional to the PCA inside eigenvector. Therefore, the residual energy between the EST negative eigenvector V_{est-} and the PCA inside eigenvector $V_{pca,in}$ is small.

A common method of measuring the difference between two sets of vectors is to project elements of one set upon the other. One way we could accomplish this is by projecting the inner image vector into the subspaces that are generated by the EST positive or PCA outside eigenvectors. The relative error energy is calculated as follows,

$$E = \frac{\left| X_{in} - \hat{X}_{in+} \right|^2}{\left| X_{in} \right|^2} \approx 1$$

where $\hat{X}_{in+}$ is the reconstruction of X_{in} using the subspace generated by the EST positive eigenvectors. However, this relative error energy is close to 1 for both target and clutter inside the inner box. This is because that the inner image vector X_{in} is almost orthogonal to the positive eigenvectors. Therefore, this is not an effective measurement. We use the following hypothesis test instead:

a. Under the null hypothesis (clutter inside), mixing of outer and inner image vectors, C_{out} and C_{in}, via EST results in a measurable change in "alignment" of EST positive and negative eigenvectors with respect to PCA inside and outside eigenvectors. That is,

$$H_0 = \left| V_{pca,in} - V_{est-} \right|^2 > \delta$$

b. Under the alternative hypothesis (target inside), mixing of outer and inner image vectors, C_{out} and C_{in}, via EST does not alter the "alignment" of EST positive and negative eigenvectors with respect to PCA inside and outside eigenvectors. That is,

$$H_1 = \left| V_{pca,in} - V_{est-} \right|^2 < \delta$$

Comparing the PCA outside eigenvector and EST positive eigenvector could also be used for exploring the differences between inner and outer image vectors. However, this analysis is in a multi-dimensional space. In the following discussion of detection criterion, we use only the PCA inside eigenvector and EST negative eigenvector.

3.3 Target Detection Procedure

The overall procedure of the target detection algorithm is outlined in the following (as shown in figure 5.)

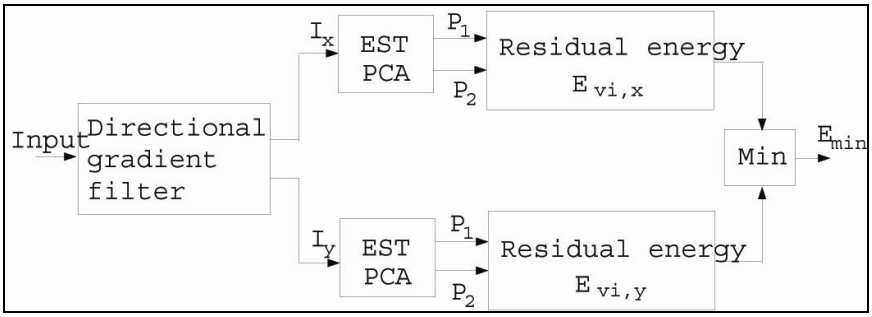

Figure 5. Procedure of the target detection algorithm.

1. The input FLIR image is passed through the gradient operators as mentioned above, to obtain two gradient images l_x and l_y, which represent the gradient images in the x and y directions, respectively.

2. For each pixel of the gradient images, the inner window and outer window are formed to obtain the inner and outer image vectors, X_{in} and X_{out}.

3. Two transformations $P_1(X_{in})$ and $P_2(X_{in}, X_{out})$ are calculated via PCA and EST, where $P_1(X_{in})$ represents the PCA positive eigenvector $V_{pca,in}$ and $P_2(X_{in}, X_{out})$ represents the EST negative eigenvector V_{est-}. That is,

$$P_1(X_{in}) = V_{pca,in}$$

$$P_2(X_{in}, X_{out}) = V_{est-}$$

4. The residual energy E_{vi} is obtained. That is,

$$E_{vi} = \left| V_{pca,in} - V_{est-} \right|^2, \quad if\ V_{pca,in} * V_{est-} > 0$$

$$E_{vi} = \left| V_{pca,in} + V_{est-} \right|^2, \quad if\ V_{pca,in} * V_{est-} < 0$$

If $V_{pca,in}$ and V_{est-} are the same sign, the residual energy is the mean square difference of these two vectors. If $V_{pca,in}$ and V_{est-} are different signs, the residual energy is the mean square sum.

5. For each pixel, two values of residual energy, $E_{vi,x}$ and $E_{vi,y}$ are calculated, corresponding to the x and y directions. The minimum of these two residual energies is retained.

$$E_{\min} = \min(E_{vi,x}, E_{vi,y})$$

6. If this minimum $E_{\min}$ is above a threshold δ, the pixel is declared clutter. If this minimum is below δ, the pixel is declared as target.

---

4. Results and Discussion

4.1 Image Database

We used two image databases yuma9207_roi and huli9204_roi from Comanche database to test the proposed target detection algorithm. Yuma9207_roi is the more difficult database because the images were taken in the summer in the Arizona desert and the background contains many high temperature spots. Huli9204_roi is an easier database. The images were taken in the spring in central California and the background is cool compared with most of the targets in the database. Figure 6 shows image examples from the two databases.

(a) (b)

Figure 6. Examples of FLIR images: (a) an image from the database yuma9207_roi, where the background contains many high temperature spots and (b) an image from the database huli9204_roi, where the background is cool compared with the targets in the image.

The proposed algorithm is based on exploring the structural differences between a target and its surroundings. For targets in a close range, the structural features of the targets are prominent within the image. For targets in a longer range image, the target appears very small and the structural information is not obvious. In order to test the algorithm performance, the algorithm is run at the different ranges. We broke the ranges down into three categories, short, medium, and long. Table 1 shows the information about these two databases. In the database, some images contain targets and some do not. When ROC curves are calculated for these databases, a roughly equal number of images, with and without targets, are randomly selected. This makes the experiment less biased.

Table 1. Database.

	Total number of image	**Number of image without targets**	**Number of image with targets**	**Range: number of images/ number of targets**
yuma9207_roi	2644	839	1805	Short range: 804/804 Medium range: 430/640 Long range: 571/1010
huli9204_roi	1910	686	1224	Short range: 971/974 Medium range: 253/403

Table 1 shows the details of the image databases. Images are stored in 10 bits. For the image database yuma9207_roi, the total number of images is 2644. Among these, the number of images without target is 839 and the number of images with target is 1805. For the images with targets, the numbers of images in short, medium, and long ranges are 803, 430, and 571, respectively. For these three ranges, numbers of targets are 804, 640, and 1010, respectively, since some images have more than one target. For the image database huli9204_roi, the total number of images is 1910, where 686 images have no targets and 1224 images have targets. For the images with targets, there are 971 images in short range, where 974 targets are found, and there are 253 images in medium range, where 403 targets are found.

4.2 ROC Results

Ideally, the proposed algorithm should calculate the residual energy at all pixels in the image. However, to reduce the computation time, the algorithm only calculates the residual energy for points that are separated in distance by a quarter of the size of the inner window. As we show in the following, this would not significantly affect the performance of the proposed algorithm.

In figure 7a, the solid line window corresponds to an inner window that is centered at a target coordinates. The bold dashed line window corresponds to one of the inner windows that our algorithm selects. Consider the ratio of the overlapping area of these two windows to the area of a single window; we call this ratio the overlapping area ratio. When this overlapping area ratio is 1, the calculating point is at the center of the target. When this overlapping area ratio is less than 1, the calculating point is away from the center of the target. Figures 7b-d show the normalized histograms of the overlapping area ratios for the images at short, medium, and long ranges, respectively, of yuma9207_roi database. From figures 7b-d, about 90% of the images have the overlapping area ratios above 0.70 at all ranges. The huli9207_roi database illustrates the similar distribution of the overlapping area ratios.

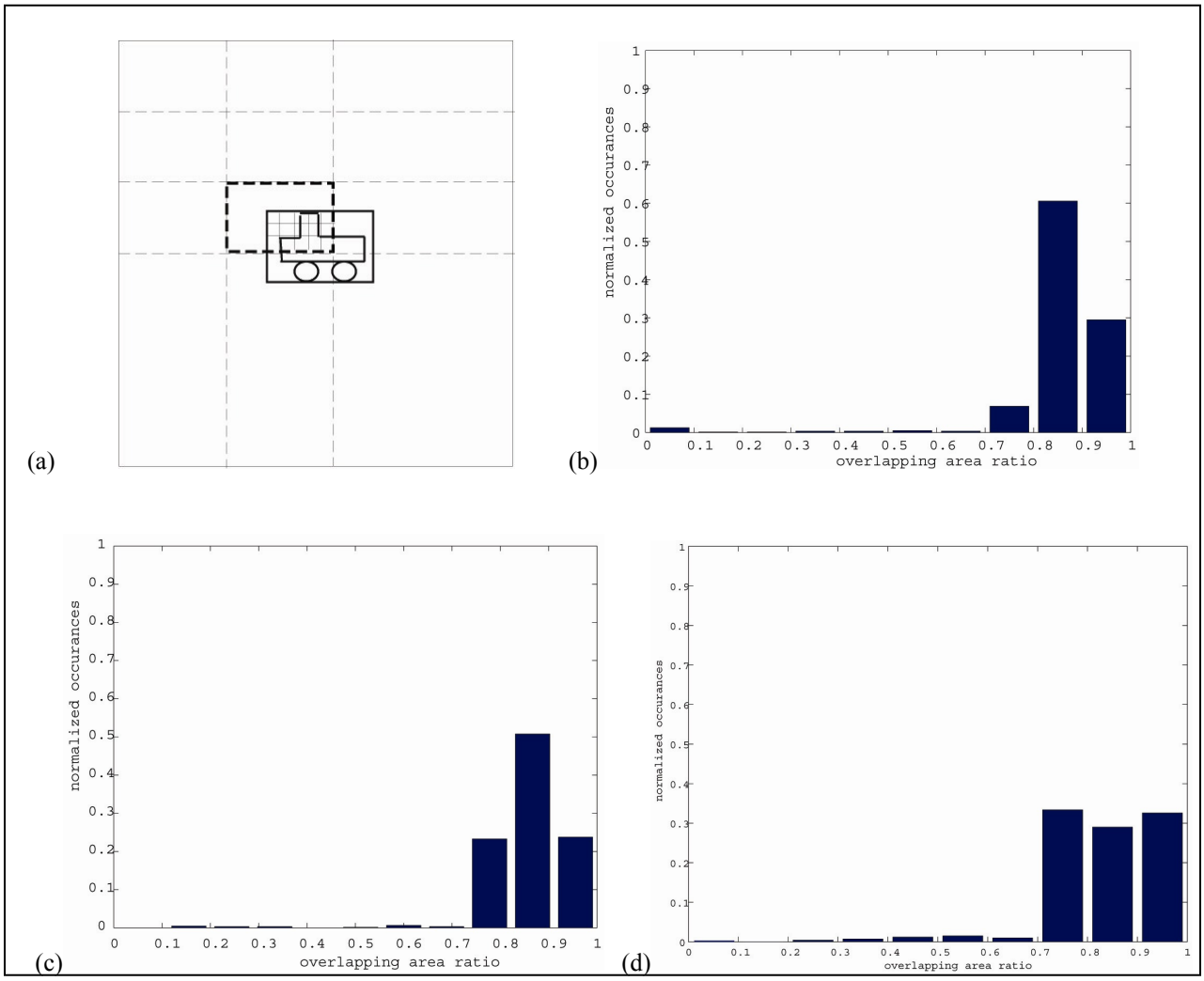

Figure 7. (a) Overlapping area ratio. The solid line window corresponds to an inner window that is centered at a target coordinates. The bold dashed line window corresponds to one of the inner windows that the algorithm selects. Overlapping area ratio is defined as the ratio of the overlapping area of these two windows to the area of a single window, (b) normalized histogram of the overlapping area ratios for short ranges, (c) normalized histogram of the overlapping area ratios for medium ranges, and (d) normalized histogram of the overlapping area ratios for long ranges.

ROC results are shown in figure 8. For the huli9204 database, as is shown in figure 8a, the two curves are for the short and medium range targets. The ROC results are very similar. For a threshold corresponding to 1 false alarm per frame (per image), the detection rate is about 81%. If the false alarm is increased to 20 per frame, the detection rate reaches 96%.

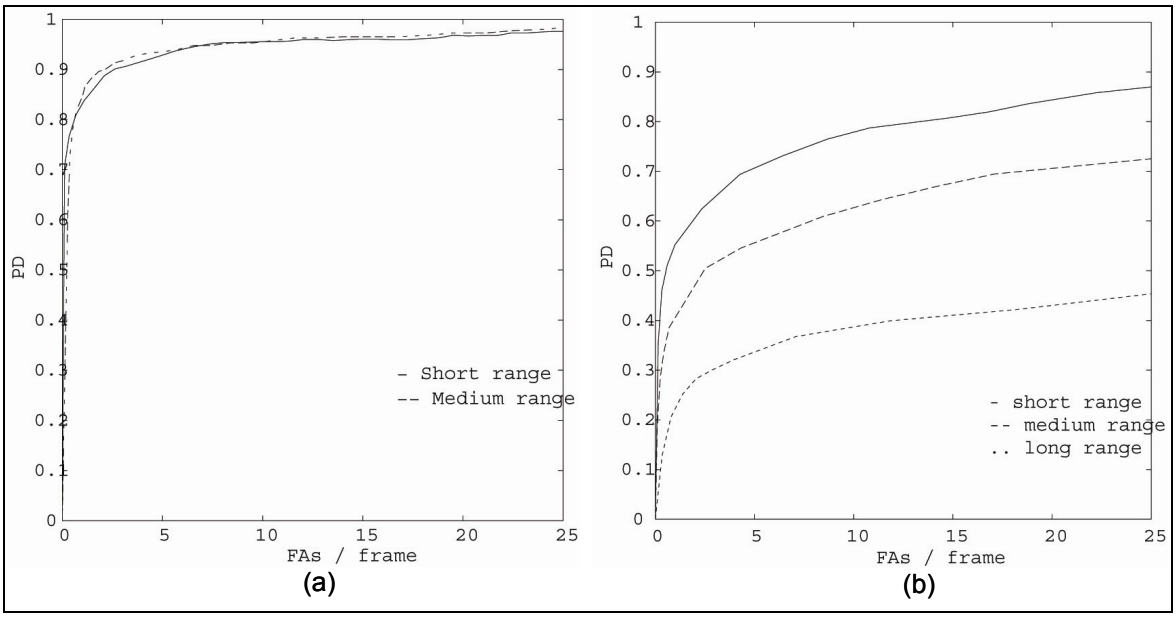

Figure 8. ROC results from the proposed implementation: (a) database huli9204_roi and (b) database yuma9207_roi.

For the yuma9207 database, as is shown in figure 8b, the ROC results are plotted for short, medium, and long ranges. The performances of these three range bins are quite different. As discussed above, for long ranges, the target appears very small in the image. In this case, there is not enough structural information available in the target chip. At 1 false alarm per frame, the detection rate is about 23%. When 20 false alarms are allowed per frame, the detection rate is about 46%. For medium ranges, the performance is improved to a detection rate of 40% for 1 false alarm per frame and 71% for 20 false alarms per frame. The best performance is achieved for short ranges. The detection rate is 58 % at 1 false alarm per frame and 84% at 20 false alarms per frame.

4.3 Discussion

As we mentioned early, to reduce the computation time, the proposed implementation only calculates the residual energy for points that are separated in distance by a quarter of size of the inner window. In order to assess the performance of this implementation, we compare this result with an ideal situation. In this ideal situation, the algorithm calculates the residual energy for points that are separated in distance with the same size as the inner window. The algorithm starts by replacing the inner window at the center of the target, which is obtained from the ground truth information. Subsequent inner windows are placed so that the inner windows are adjacent, non-overlapping, and cover as much of the image as is possible consistent with both inner and outer windows being completely contained within the image.

Figure 9 shows the ROC results for the proposed implementation and the ideal situation for the database yuma9207_roi. Figure 9a shows the results for 0 to 25 false alarms per frame. Figure

9b shows the enlarged portion of the false alarm rates between 0 to 5. The solid lines are the ROC results for the ideal situation. The dash lines are the ROC results for the proposed implementation that is obtained in figure 8b. The upper lines in the figure are ROC results for the short ranges, the middle lines are for the medium ranges, and lower lines are for the long ranges. The overall results show that similar results are obtained from the proposed implementation and the ideal situation. For the long ranges, the detection rate of the proposed implementation is 23% versus 25% of the ideal situation at 1 false alarm per frame, and 46% versus 48% at 20 false alarms per frame. For the medium ranges, at 1 false alarm rate, the detection rates of the proposed implementation and the ideal situation are 40% and 49%, respectively; at 20 false alarms per frame, 71% and 72%, respectively. For the short ranges, at 1 false alarm per frame, the detection rates of the proposed implementation and the ideal situation are 58% and 63%, respectively; at 20 false alarms per frame, 84% and 85%, respectively.

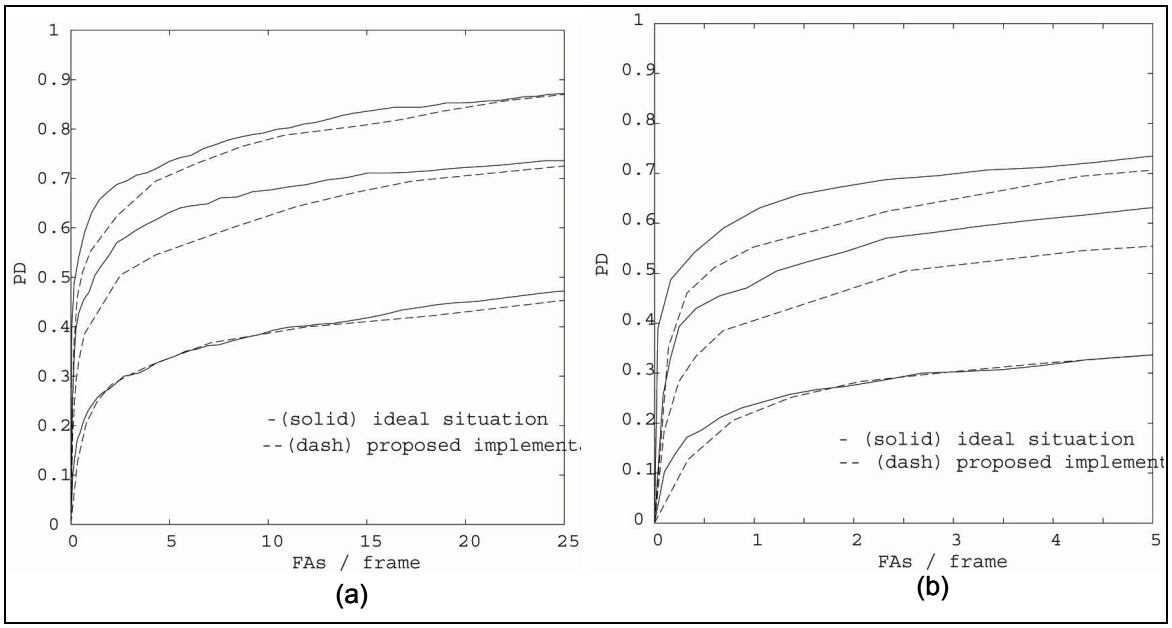

Figure 9. ROC results of the proposed implementation comparing with the ideal situation for the database yuma9207_roi: (a) ROC results of false alarm rates between 0 and 25; (b) ROC results of false alarm rates between 0 and 5.

This result demonstrates that the algorithm performance is not significantly changed when the center of the inner window is not exactly located at the center of the target. However, the measure of closeness of the center of the inner window and the center of the target is required to be within a certain degree. For example, the overlapping area ratio that was defined above needs to be over 0.70 as shown here.

The proposed algorithm is also compared with another target detection algorithm, called spatial anomaly detection algorithm (SADA) which was described in [*19*], for the database yuma9207. The ROC curves are shown in figures 10a-b. Figure 10a shows the results for 0 to 25 false alarms per frame. Figure 10b shows the enlarged portion of the false alarm rates between 0 and

5. The solid lines represent the results for the SADA algorithm and the dash lines are for proposed algorithm. The upper lines in the figure are ROC results for the short ranges, the middle lines are for the medium ranges, and the lower lines are for the long ranges. The overall results show that the proposed algorithm has a higher detection performance than the SADA at low false alarm rates. At higher false alarm rates, the SADA gives slightly higher detection rates. See figure 10b; at short ranges, the detection rates of the proposed algorithm and the SADA are similar. For medium ranges, at 1 false alarm per frame, the detection rate of the proposed algorithm is 40% from the 29% obtained by the SADA. For long ranges, at 1 false alarm per frame, the detection rate of the proposed algorithm is increased to 23% from 18% obtained by the SADA.

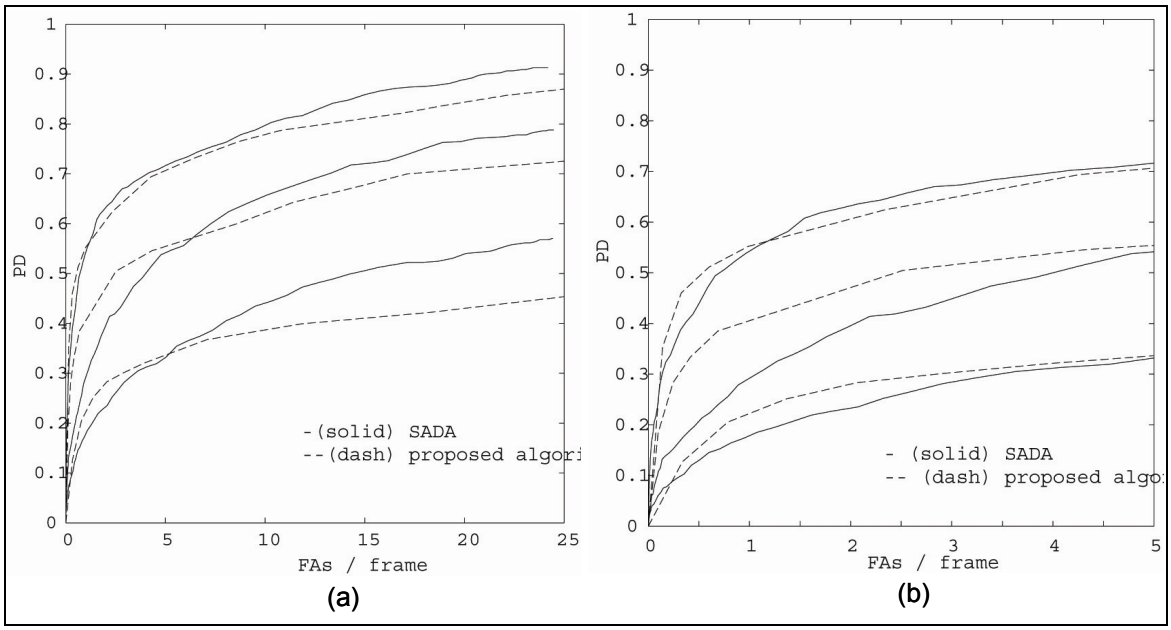

Figure 10. ROC results of the proposed algorithm comparing with the SADA for the database yuma9207_roi: (a) ROC results of false alarm rates between 0 and 25 and (b) ROC results of false alarm rates between 0 and 5.

The results of testing on each point for two images (both containing one target) showed that the hit points are concentrated in the target area, suggesting that the performance of the algorithm does not deteriorate significantly by not testing on every image point. Detection results obtained by testing each point on one image are shown in figures 11a-c. Figure 11a shows the gradient image obtained by highpass filtering the FLIR image in the x direction. The values of the residual energy $E_{\min}$ are displayed as the image gray-level values in figure 11b. The image is displayed in an inverse mode such that the lower $E_{\min}$ values appear brighter. All brighter areas appear in the target area and the transition areas between vegetation and ground, where strong structural information exists. In figure 11c, the points with $E_{\min}$ values that are less than the threshold (0.3 in this case) are superimposed into the gradient image. All hit points are within the target area.

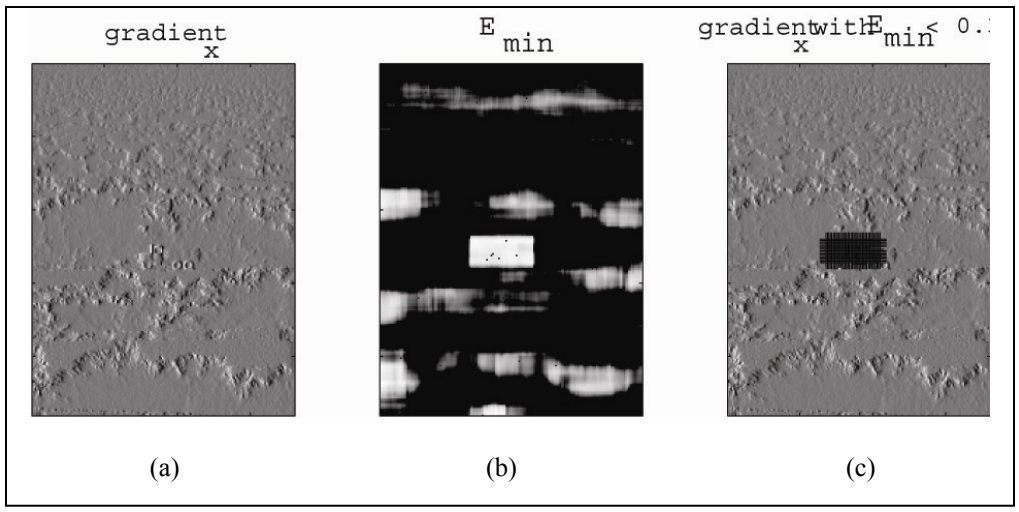

Figure 11. Detection results: (a) gradient image obtained by the highpass filtering in the x direction, (b) residual energy E_{min} values, and (c) the points with $E_{min} < 0.3$ are superimposed into the gradient image in (a) as markers (+).

As discussed earlier, the range between a target and the sensor changes the target structural information that appears in FLIR images. The proposed algorithm is designed to detect targets that appear at short and medium ranges within the FLIR imagery. For targets at long ranges (where targets appear as "blob" if it is hot), a different algorithm (such as an energy detector), that does not rely on a detailed structural information, is needed.

5. Conclusions

An adaptive target detection algorithm based on exploiting the structural information within a target and its background is presented. The algorithm calculates the inner and outer image gradient vectors representing the target and its background, respectively. The EST and PCA transforms are locally generated from the inner and outer image gradient vectors. The differences between the EST and PCA eigenvectors are used to distinguish the target from its background. Results of testing the proposed algorithm on two large FLIR databases were presented.

6. References

1. Lloyd, J. M. *Thermal imaging systems*, New York: Plenum, 1982.

2. Wolfe, W. L.; Zissis, G. J. Eds. *The Infrared Handbook*, Erim International, 1985.

3. Ratches, J. A.; Vollmerhausen, R. H.; Driggers, R. G. Target acquisition performance modeling of infrared imaging systems: past, present, and future. *IEEE Sensors Journal* **2001**, *1* (1), 31–40.

4. Bhanu, B.; Jones, T. L. Image Understanding research for automatic target recognition. *IEEE AES Systems Magazine* **October 15–22 1993**.

5. Bhanu, B. Automatic target recognition: state of art survey. *IEEE Trans. on Aerospace and Electronic Systems* **1986**, *AES-22* (4), 364–379.

6. Sang, N.; Zhang, T. Segmentation of FLIR images by Hopfield neural network with edge constraint. *Pattern Recognition* **2001**, *34*, 811–821.

7. Sun, S-G.; Park, H. Segmentation of forward-looking infrared image using fuzzy thresholding and edge detection. *Optical Engineering* **2001**, *40* (11), 2638–2645.

8. Ernisse, B.; Rogers, S. K.; DeSimio, M. P.; Raines, R. A. Complete automatic target cuer/recognition system for tactical forward-looking infrared images. *Optical Engineering* **1997**, *36* (9), 2593–2603.

9. Park, S-I.; Murenzi, R.; Smith, M.J.T. Multidimensional wavelets for target detection and recognition. *Wavelet Applications III (8-12 April 1996 : Orlando, FL, USA*, *Proceedings of the SPIE* 2762, 177–187, 1996.

10. Zhou Y. T.; Crawshaw, R. Contrast, size and orientation invariant target detection in infrared imagery. *Automatic Object Recognition, Proceedings of SPIE* 1471, 1991.

11. Weber, D. M.; Casasent, D. P. Quadratic Gabor filters for object detection. *IEEE Trans. on Image Processing* **2001**, *10* (2), 218–230.

12. Roth, M. W. Survey of neural network technology for automatic target recognition. *IEEE Trans. on Neural Networks* **1990**, *1* (1), 28–43.

13. Rizvi, S. A.; Nasrabadi, N. M. Neural network algorithms for automatic target recognition using forward-looking infra-red imagery: A Survey. *PINSA* **2001**, *67A* (2), 243–276.

14. Dwan, C. M.; Der, S. Z. A neural network based target detection system for FLIR imagery. Applications of Artificial Neural Networks in Image Processing III (26-27 Jan. 1998: San Jose, CA, USA). *Proceedings of the SPIE 3307*, 14–21, 1998.

15. Ramanan, S.; Peterson, R. S.; Clarkson T. G.; Taylor, J. G. pRAM nets for detection of small targets in sequences of infra-red images. *Neural Networks* **1995**, *8* (7/8), 1227–1237.

16. Xue, D-H.; Zhu, Y-T.; Zhu, G-X; Xiong, Y. Recognition of low-contrast FLIR tank object on multiscale fractal character vector. *Automatic Object Recognition VI: (9–10 April 1996, Orlendo, FL, USA), Proceedings of SPIE* 2756, 38–45, 1996.

17. Shekarforoush, H.; Chellappa, R. A multi-fractal formalism for stabilization, object detection and tracking in FLIR sequences. *Proceedings 2000 International Conference on Image Processing, Piscataway, NJ, USA*, Vol 3, 78–81, 2000.

18. Gregois, D. J.; Yu, S.K.W.; Tritchew, S.; Sevigny, L. Wavelet transformation-based filtering for the enhancement of dim targets in FLIR images. *Wavelet Applications (5-8 April 1994: Orlando, FL, USA), Proceedings of SPIE* 2242, 573–583, 1994.

19. Der, S.; Nasrabadi, N.; Chan, A.; Kwon, H. Spatial Anomaly detection algorithm for FLIR imagery. *Advances in Imaging Sciences and Engineering: Algorithms, Systems, and Applications*, edited by Bahram Javidi, Spring-Verlag, 2002.

20. Torrieri, D. The eigenspace separation transform for neural-network classifiers. *Neural Networks* **1999**, *12*, 419–427.

21. Krauskopf, J. Effect of retinal image stabilization on the appearance of heterochromatic targets. *Journal of the Optical Society of America* **1963**, *53*, 741–744.

22. Hubel, D. H. *Eye, Brain, and Vision*, Scientific American Library, W. H. Freeman, New York, 1988.

Distribution List

ADMNSTR
DEFNS TECHL INFO CTR
ATTN DTIC-OCP (ELECTRONIC COPY)
8725 JOHN J KINGMAN RD STE 0944
FT BELVOIR VA 22060-6218

DARPA
ATTN IXO S WELBY
3701 N FAIRFAX DR
ARLINGTON VA 22203-1714

OFC OF THE SECY OF DEFNS
ATTN ODDRE (R&AT)
THE PENTAGON
WASHINGTON DC 20301-3080

US ARMY TRADOC
BATTLE LAB INTEGRATION & TECHL DIRCTRT
ATTN ATCD-B
10 WHISTLER LANE
FT MONROE VA 23651-5850

US MILITARY ACDMY
MATHEMATICAL SCI CTR OF EXCELLENCE
ATTN MADN-MATH LTC T RUGENSTEIN
THAYER HALL RM 226C
WEST POINT NY 10996-1786

SMC/GPA
2420 VELA WAY STE 1866
EL SEGUNDO CA 90245-4659

US ARMY ARDEC
ATTN AMSTA-AR-TD
BLDG 1
PICATINNY ARSENAL NJ 07806-5000

COMMANDING GENERAL
US ARMY AVN & MIS CMND
ATTN AMSAM-RD W C MCCORKLE
REDSTONE ARSENAL AL 35898-5000

US ARMY INFO SYS ENGRG CMND
ATTN AMSEL-IE-TD F JENIA
FT HUACHUCA AZ 85613-5300

US ARMY NATICK RDEC
ACTING TECHL DIR
ATTN SBCN-TP P BRANDLER
KANSAS STREET BLDG 78
NATICK MA 01760-5056

US ARMY SIMULATION TRAIN & INSTRMNTN CMND
ATTN AMSTI-CG M MACEDONIA
12350 RESEARCH PARKWAY
ORLANDO FL 32826-3726

US GOVERNMENT PRINT OFF
DEPOSITORY RECEIVING SECTION
ATTN MAIL STOP IDAD J TATE
732 NORTH CAPITOL ST., NW
WASHINGTON DC 20402

HICKS & ASSOC INC
ATTN G SINGLEY III
1710 GOODRICH DR STE 1300
MCLEAN VA 22102

US ARMY RSRCH LAB
ATTN AMSRD-ARL-CI-OK-TP TECHL LIB
T LANDFRIED
ABERDEEN PROVING GROUND MD 21005-5066

DIRECTOR
US ARMY RSRCH LAB
ATTN AMSRD-ARL-RO-D JCI CHANG
ATTN AMSRD-ARL-RO-EN W D BACH
PO BOX 12211
RESEARCH TRIANGLE PARK NC 27709

US ARMY RSRCH LAB
ATTN AMSRD-ARL-D J M MILLER
ATTN AMSRD-ARL-CI-OK-T TECHL PUB (2 COPIES)
ATTN AMSRD-ARL-CI-OK-TL TECHL LIB (2 COPIES)
ATTN AMSRD-ARL-SE-SE S S YOUNG (7 COPIES)
ATTN IMNE-ALC-IMS MAIL & RECORDS MGMT
ADELPHI MD 20783-1197